nature materials

ARTICLES

https://doi.org/10.1038/s41563-019-0562-6

Quantitative production of butenes from biomass-derived γ-valerolactone catalysed by hetero-atomic MFI zeolite

Longfei Lin[1], Alena M. Sheveleva[1,2], Ivan da Silva[3], Christopher M. A. Parlett[4,5,6], Zhimou Tang[7], Yueming Liu[7], Mengtian Fan[1], Xue Han[1], Joseph H. Carter[1], Floriana Tuna[1], Eric J. L. McInnes[1], Yongqiang Cheng[8], Luke L. Daemen[8], Svemir Rudić[3], Anibal J. Ramirez-Cuesta[8], Chiu C. Tang[6] and Sihai Yang[1*]

The efficient production of light olefins from renewable biomass is a vital and challenging target to achieve future sustainable chemical processes. Here we report a hetero-atomic MFI-type zeolite (NbAlS-1), over which aqueous solutions of γ-valerolactone (GVL), obtained from biomass-derived carbohydrates, can be quantitatively converted into butenes with a yield of >99% at ambient pressure under continuous flow conditions. NbAlS-1 incorporates simultaneously niobium(v) and aluminium(iii) centres into the framework and thus has a desirable distribution of Lewis and Brønsted acid sites with optimal strength. Synchrotron X-ray diffraction and absorption spectroscopy show that there is cooperativity between Nb(v) and the Brønsted acid sites on the confined adsorption of GVL, whereas the catalytic mechanism for the conversion of the confined GVL into butenes is revealed by in situ inelastic neutron scattering, coupled with modelling. This study offers a prospect for the sustainable production of butene as a platform chemical for the manufacture of renewable materials.

Approximately 400 million tonnes of light olefins (ethene, propene and butenes) are produced each year for polymer, chemical and pharmaceutical industries[1–6]. State-of-the-art processes are based on the stream cracking of naphtha and thus critically rely on fossil fuels, which possess significant environmental impacts[1]. The catalytic production of light olefins from renewable plant biomass is a highly promising target[7], and many processes have been developed to bridge future gaps in the supply of commodity chemicals from biomass[8–11]. In particular, biomass-derived γ-valerolactone (GVL), obtained from agricultural waste via low-cost, high-yield commercial processes (production scale at 27 tonnes in 2018), was identified as a sustainable resource to produce butenes[12], which, through well-established petroleum processes, can be readily transformed into a wide spectrum of petrochemicals, such as propene[2,13], 1,3-butadiene[14], aromatics[15], liquid fuels[2,9], polyethylene[2,16] and polybutene[2,17]. In this respect, the development of efficient catalytic processes to convert GVL into butenes is of vital importance. This conversion involves the ring opening and decarboxylation reactions catalysed over solid acids, and amorphous SiO_2/Al_2O_3, ZSM-5, La/ZSM-5, Ni_2P/MCM-41, Zn-AlPO-5 and Pd/Nb_2O_5 have been studied[9,15,18–24]. Using a 30 wt% GVL feedstock at 375 °C and atmospheric pressure, a butene yield of 75% has been achieved over the SiO_2/Al_2O_3 catalyst[9]. Commercial supplies of GVL from biorefineries are aqueous solutions with GVL concentrations between 20 and 40 wt% (ref. [15]); however, the water in the reaction can partially or completely deactivate solid acid catalysts by coordinating to the acid sites and forming acid–base adducts[25,26]. Thus, the design of an efficient, yet water-tolerant, catalyst for this conversion remains a fundamental challenge. Recently, emerging niobium-based catalysts were shown to possess a marked water tolerance[25–32] and exceptional activities for the hydrodeoxygenation of biomass under mild conditions[33–35].

Here we describe the development of a hetero-atomic MFI-type zeolite (denoted as NbAlS-1) and its catalytic activity for the conversion of GVL into butenes. NbAlS-1 integrates both Nb(v) and Al(iii) sites into the framework, and through fine-tuning of the ratio of Nb:Al:Si, the optimal acidity and hence reactivity of the catalyst can be achieved to promote a quantitative production of butenes (yield >99%) using a 30 wt% GVL feedstock at 320 °C and atmospheric pressure in the absence of an external source of hydrogen. NbAlS-1 shows a superior water tolerance and catalytic stability over 180 hours in a continuous-flow reaction. The underlying catalytic mechanism was elucidated at a molecular level, employing a combination of in situ synchrotron X-ray powder diffraction (SXPD), X-ray absorption spectroscopy (XAS), inelastic neutron scattering (INS) and density functional theory (DFT) calculations. These complimentary techniques revealed that the cooperativity between Nb(v) and Brønsted acid sites plays a key role in the reactivity of GVL and, compared with conventional HZSM-5, the absence of strong Brønsted acid sites in NbAlS-1 effectively hindered the formation of by-products, which results in the observed selectivity for butenes.

[1]Department of Chemistry and Photon Science Institute, University of Manchester, Manchester, UK. [2]International Tomography Centre SB RAS and Novosibirsk State University, Novosibirsk, Russia. [3]ISIS Facility, STFC, Rutherford Appleton Laboratory, Chilton, UK. [4]School of Chemical Engineering and Analytical Science, University of Manchester, Manchester, UK. [5]University of Manchester at Harwell, Diamond Light Source, Harwell Campus, Didcot, UK. [6]Diamond Light Source, Harwell Science and Innovation Campus, Didcot, UK. [7]Shanghai Key Laboratory of Green Chemistry and Chemical Processes, School of Chemistry and Molecular Engineering, East China Normal University, Shanghai, China. [8]The Chemical and Engineering Materials Division (CEMD), Neutron Sciences Directorate, Oak Ridge National Laboratory, Oak Ridge, TN, USA. *e-mail: Sihai.Yang@manchester.ac.uk

Synthesis and characterization

The hydrothermal synthesis of ZSM-5 doped with varying loadings of Nb(v) (0–5.58 wt%) and Al(III) (0–1.64 wt%) was systematically studied, and all the obtained materials exhibit the MFI-type framework (Supplementary Fig. 1), BET surface areas of 357–408 $m^2 g^{-1}$ (Supplementary Table 1) and particle size distributions between 300 and 500 nm (Supplementary Fig. 2 and Supplementary Table 1). All the zeolites studied here exhibit similar micropore volumes (Supplementary Table 1). An optimal loading of 3.81 wt% Nb(v) and 1.64 wt% Al(III) was identified for the synthesis of NbAlS-1(0.027/0.04/1) (yield = 95%). The atomic ratio of Nb/Al/Si was determined by energy-dispersive X-ray (EDX) analysis to be 0.027/0.04/1 with a homogeneous distributions of metal ions (Fig. 1a–e). The vibrational modes of the Nb–O–Si moieties[36] in NbAlS-1(0.027/0.04/1) were observed by Fourier transform infrared (FTIR) spectroscopy (971 cm^{-1}; Fig. 1f) and Raman spectroscopy (921 and 973 cm^{-1}; Fig. 1g), which indicates the incorporation of Nb(v) centres as the framework T sites.

The successful incorporation of Nb(v) and Al(III) into framework sites was further confirmed by electron paramagnetic resonance (EPR) spectroscopy. Although NbS-1 (the isostructural analogue with 0% Al loading) and NbAlS-1 are EPR silent due to the diamagnetic Nb(v) and Al(III) ions, characteristic paramagnetic centres can be induced by γ-irradiation of the zeolites[36]. EPR spectra of γ-irradiated NbS-1(0.027/1) and NbAlS-1(0.027/0.04/1) show a wide, structured signal that spreads over a magnetic field range of ~350 mT (Fig. 1h) with a ten-line hyperfine structure, consistent with the coupling of an unpaired electron to a ^{93}Nb nucleus ($I = 9/2$, 100% natural abundance). The site has axial symmetry with g values of $g_{\|} = 1.866$ and $g_{\perp} = 1.935$, and hyperfine couplings of $A^{Nb}_{\|} = 0.0289\ cm^{-1}$ and $A^{Nb}_{\perp} = 0.0148\ cm^{-1}$ (Supplementary Table 2), consistent with the previous characterization of Nb(IV) centres generated at the pseudo-tetrahedral NbO_4 units in the framework of silicalite-1[36], whereas this signal is not observed in γ-irradiated HZSM-5 or Nb_2O_5-HZSM-5 mixtures (Fig. 1h), indicative that the Nb(v) ion in NbAlS-1 is solely incorporated into framework sites, rather than deposited as Nb_2O_5 phases. A second narrow signal with a hyperfine structure observed in the spectra of γ-irradiated HZSM-5 and NbAlS-1 (Fig. 1i and Supplementary Table 2) arises from an electron hole defect on a framework oxygen atom in an Al–O•–Si site[37], where the structure arises from hyperfine coupling with the ^{27}Al nucleus ($I = 5/2$, 100% natural abundance). In γ-irradiated NbS-1, a sharp signal is observed, but the hyperfine structure is lost, consistent with the absence of Al(III). Thus, EPR measurements provide convincing evidence for the incorporation of both Nb(v) and Al(III) into framework sites in NbAlS-1, which enables the fine-tuning of its framework acidity and hence catalytic activity.

Pyridine-adsorption FTIR (Py-IR) spectroscopy has been used to characterize the nature of acidity in these zeolites (Supplementary Fig. 3 and Supplementary Table 3). NbS-1 exhibits solely Lewis acidity due to the presence of Nb(v), whereas NbAlS-1 shows both Lewis and Brønsted acidity, which arises from the dual functionality of Nb(v) and Al(III) sites. Notably, the nature of the acidity in NbAlS-1 is distinct to that of HZSM-5: the ratio of Lewis/Brønsted acid sites in NbAlS-1 is 4.69, 12 times that of HZSM-5. The acidity was quantified by ammonia temperature-programmed desorption (Supplementary Fig. 4 and Supplementary Table 3). HZSM-5 displays both strong and weak acid sites with a total amount of 0.4–0.63 mmol g^{-1} and NbS-1 exhibits minor weak acid sites of 0.04 mmol g^{-1}. Interestingly, NbAlS-1 shows only weak acid sites, but their concentration is considerably higher (0.22 mmol g^{-1}) than that of NbS-1. Thus, doping of pentavalent niobium sites into the zeolite can effectively tune the nature and distribution of framework acidity and provides an excellent platform to examine the resultant catalytic activities.

Catalytic tests

Conversions of pure GVL were firstly performed over a fixed-bed packed with the catalysts under flow conditions at 320 °C (weight hourly space velocity = 0.18 h^{-1}; Table 1). HZSM-5 with varying Al/Si ratios shows GVL conversions of 75–92% and moderate butene yields of 33.1–44.1% (Table 1, entries 1–3). This is due to the formation of considerable amounts of 2-cyclopentenone, aromatics and polycyclic aromatics as by-products and coke over strong acid sites (Supplementary Figs. 5 and 6). However, the lack of Brønsted acid sites in NbS-1 gives very low butene yields (~7%) and GVL conversions (32%) (Table 1, entries 4 and 5). In contrast, a 96% GVL conversion with an 80.4% butene yield was achieved over NbAlS-1 (0.027/0.04/1) (Table 1, entry 6). This suggests that the strength and nature of the framework acidity are key parameters for optimizing its performance. By introducing Nb(v) as weak Lewis acid sites to weaken the strong Al(III) acid sites in NbAlS-1, the formation of by-products was effectively inhibited, which leads to high selectivities for butenes over NbAlS-1.

The catalytic performance of these zeolites was further tested using 30 and 60 wt% aqueous solutions of GVL (Table 1 and Supplementary Table 4); the former is of direct relevance to practical processes[15]. The butene yields from aqueous solutions of GVL over HZSM-5 with varying Si/Al ratios decreased to 22.2–29.2% owing to the deactivation of acid sites in the presence of water (Table 1, entries 1–3, 11 and 13–15). Significantly, a quantitative production of butenes (yield > 99%) was achieved over NbAlS-1(0.027/0.04/1) using a 30 wt% GVL feedstock (Table 1, entry 16), which demonstrates the significantly improved water tolerance by Nb(v) doping. Other widely studied Nb-containing catalysts, such as Nb_2O_5, niobic acid ($Nb_2O_5 \cdot H_2O$) and $NbOPO_4$, were also tested for this reaction and, as expected, these catalysts all exhibited excellent water tolerance (Table 1, entries 8–10 and 17–19). A butene yield of 78.3% was obtained from the conversion of 30 wt% aqueous solutions of GVL over $NbOPO_4$, which, however, has a much lower utilization efficiency of Nb compared with NbAlS-1(0.027/0.04/1) (46% and 3.8%, respectively, in terms of Nb concentration). The performance of NbAlS-1(0.027/0.04/1) compares favourably with state-of-the-art catalysts (Supplementary Table 5). As previously observed in niobic acid systems, water can only partially coordinate to the Nb(v) centres, which leaves sufficient positive charges on NbO_4 moieties to bind substrates[26,31]. Indeed, the formation of coke, 2-cyclopentenone and other by-products is effectively inhibited over NbAlS-1(0.027/0.04/1) by the presence of water (Table 1 and Supplementary Fig. 7). The excellent stability of NbAlS-1(0.027/0.04/1) was demonstrated by both cycling and time-on-stream tests, in which the yield of butenes remained at >99% after 180 hours of reaction (Fig. 2a,b). The used catalyst was characterized by N_2 sorption, synchrotron XPD, EDX analysis, FTIR spectroscopy, EPR spectroscopy (on ^{60}Co γ-irradiation), XAS, ^{27}Al NMR spectroscopy, ammonia temperature-programmed desorption and Py-IR spectroscopy (Fig. 2c,d and Supplementary Figs. 8–12). Importantly, all these results confirm that there is little change to the structure and acidic sites of used NbAlS-1, which demonstrates the excellent structural stability of the bifunctional zeolite. Interestingly, little change was observed in the structure and acidic sites of the used HZSM-5(0.04/1) (Fig. 2c,d and Supplementary Figs. 11–13), which indicates that the decrease of catalytic activity of HZSM-5 on exposure to water compared with reactions using pure GVL (Table 1, entries 2, 11 and 14) is primarily due to partial poisoning of the acidic sites, consistent with the literature[25,26].

Studies of the coordination environment of Nb(v) sites

To understand the effect of active Nb(v) sites, their local environment was interrogated through Nb K-edge XAS. The absorption edge positions for both NbAlS-1(0.027/0.04/1) and NbS-1(0.027/1) from X-ray absorption near-edge spectra are consistent with the pentavalent oxidation state[38] with as-prepared samples that exhibit a

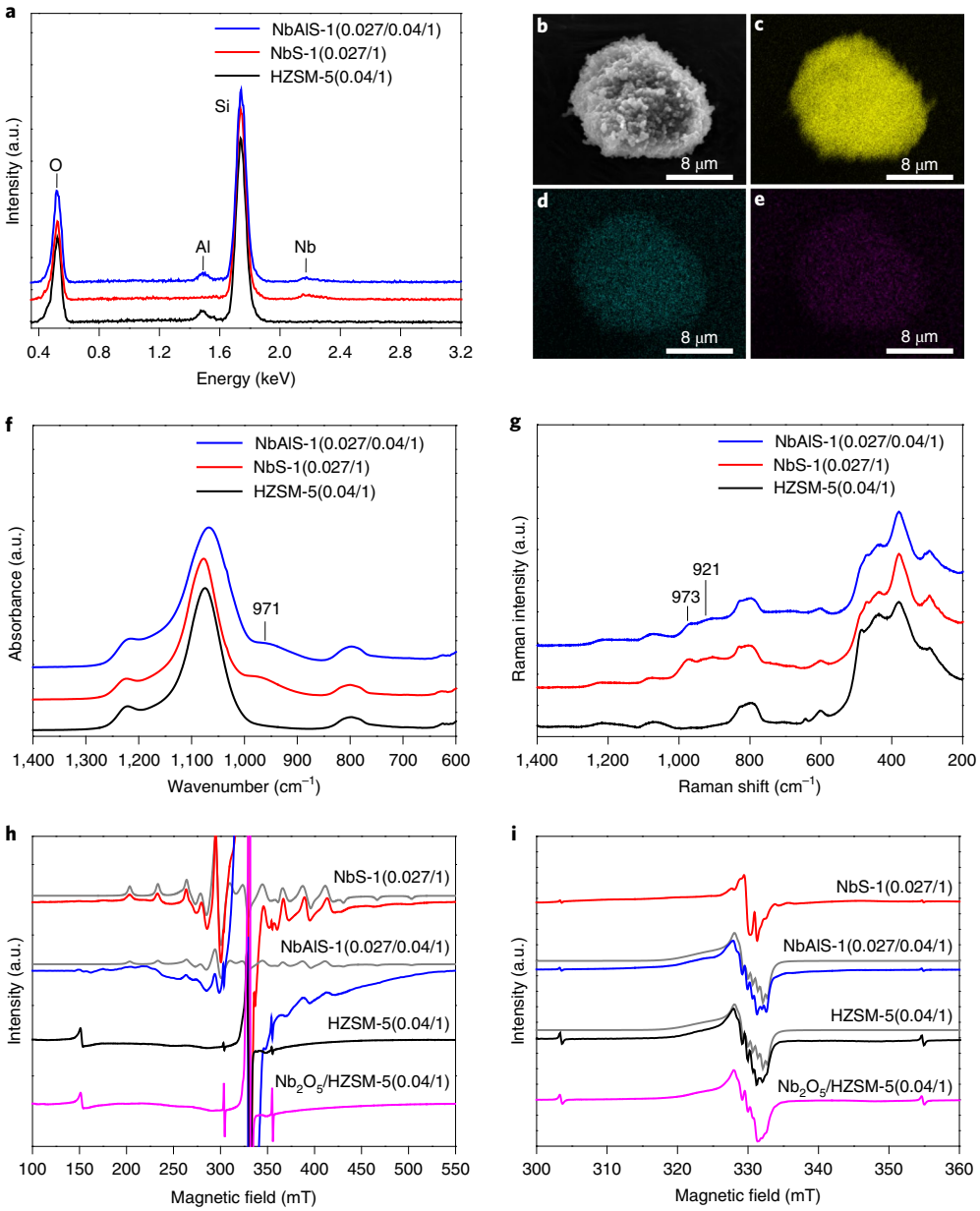

Fig. 1 | Physical characterization of catalysts. a, EDX spectra of HZSM-5(0.04/1), NbS-1(0.027/1) and NbAlS-1(0.027/0.04/1). The peaks in the regions of 0.52, 1.49, 1.74 and 2.17 keV are related to the binding energies of O Kα, Al Kα, Si Kα and Nb Lα, respectively. **b**, Scanning electron microscopy image of NbAlS-1(0.027/0.04/1). **c**–**e**, EDX maps of Si Kα (**c**), Al Kα (**d**) and Nb Lα (**e**) in NbAlS-1(0.027/0.04/1). **f**,**g**, FTIR (**f**) and Raman (**g**) spectra of HZSM-5(0.04/1), NbS-1(0.027/1) and NbAlS-1(0.027/0.04/1) samples. **h**,**i**, X-band (~9 GHz) EPR spectra of activated zeolites by γ-irradiation at 77 K: the wide magnetic field sweep (**h**) highlights the induced Nb(IV) signals in NbS-1(0.027/1) and NbAlS-1(0.027/0.04/1) and the narrow magnetic field-sweep (**i**) highlights the induced electron hole defect Al–O•–Si signals in NbAlS-1(0.027/0.04/1) and HZSM-5(0.04/1). The weak features at ~304 and 356 mT in **i** are due to radiation-induced trapped hydrogen atoms. The experimental spectra are shown in black, red, blue and magenta. The simulated spectra of Nb(IV) (**h**) and Al–O•–Si (**i**) defects are shown in grey. a.u., arbitrary units.

common weak pre-edge peak (Fig. 3a). The weak nature of this pre-edge feature can be attributed to disruption of the pseudo-tetrahedral Nb environment via water coordination (Fig. 3b)[38]. On adsorption of GVL to the pores of NbAlS-1, the pre-edge position was further influenced with an apparent blueshift (~0.8 eV); in contrast, no shift was witnessed for NbS-1. This reflects both a greater electron donation from GVL[39] and the preferred adsorption geometry within the bifunctional zeolite NbAlS-1, which facilitates a closer interaction between the Nb(v) sites and the substrate. This conclusion was verified through extended X-ray absorption fine structure analysis (Fig. 3c). Fitting of the first coordination shell revealed an increase in the average Nb=O bond length due to the presence of an adsorbate and a subsequent decrease in the double-bond nature, whereas the siloxane bridges remain unaffected (Supplementary Table 6). The effect was apparent in both the NbAlS-1 and NbS-1 systems, and the NbAlS-1 system was perturbed to a significantly greater extent, 0.22 versus 0.06 Å increase in bond length, respectively. Furthermore, fitting of the second coordination shell discredited the potential for bulk Nb_2O_5 formation, which confirmed the location of Nb(v) to be solely within the framework, consistent with the EPR observation. Thus, the framework Nb(v) site plays a key role in the adsorption of GVL in NbAlS-1.

Table 1 | Summary of the GVL conversion and product yields over different catalysts[a]

Entry	Catalyst	GVL concentration (wt%)	GVL conversion (%)	Yield (mol %)			
				Butene	2-cyclopentenone	Aromatics	Others[b]
1	HZSM-5(0.027/1)	99	75	33.1	9.9	10.3	21.7
2	HZSM-5(0.04/1)	99	83	37.9	11.5	12.4	21.2
3	HZSM-5(0.067/1)	99	92	44.1	13.4	12.9	21.6
4	NbS-1(0.027/1)	99	31	6.9	0.4	0	23.7
5	NbS-1(0.04/1)	99	32	7.2	0.4	0	24.4
6	NbAlS-1(0.027/0.04/1)	99	96	80.4	6.2	0.2	9.2
7	NbAlS-1(0.04/0.027/1)	99	84	56.3	4	0.2	23.5
8	Nb_2O_5	99	8	6.9	0	0	1.1
9	$Nb_2O_5{\cdot}nH_2O$	99	36	15.8	0.9	0	19.3
10	$NbOPO_4$	99	75	47.2	5.3	0.5	22.0
11	HZSM-5(0.04/1)	60	81	29.2	9.3	9.2	33.3
12	NbAlS-1(0.027/0.04/1)	60	100	92.3	0.3	0	7.4
13	HZSM-5(0.027/1)	30	73	22.2	6.3	6.7	37.8
14	HZSM-5(0.04/1)	30	76	23.2	4.7	7.1	41.0
15	HZSM-5(0.067/1)	30	85	23.3	4.6	7.4	49.7
16	NbAlS-1(0.027/0.04/1)	30	100	99.3	0	0	0.7
17	Nb_2O_5	30	11	10.1	0	0	0.9
18	$Nb_2O_5{\cdot}nH_2O$	30	38	20.0	2.3	0	15.7
19	$NbOPO_4$	30	88	78.3	0	0	9.7

[a]Reaction conditions: catalyst, 2.0 g; reaction temperature, 320 °C; atmospheric pressure; weight hourly space velocity, 0.18 h^{-1}; time-on-stream, 10 h. [b]Other products include C_2–C_4 hydrocarbons (except butene), pentenoic acid isomers, 1-(2-methylcyclopropyl)ethanone, 3,3-diethoxy-1-propyne, cyclobutanecarboxylic acid-2-propenyl ester, 3-methyl-2-butenoic acid, cyclobutyl ester (the latter four compounds are mainly for entries 4 and 5), 4-ethyl-4-methyl-2-cyclohexene-1-one (detected for entries 9, 10, 18 and 19), 3-ethyl-1-isopropyl-1H-indene (detected for entries 10 and 19) and polycyclic aromatics.

Determination of adsorption domains for GVL

The binding domains of GVL within these zeolites were determined from in situ SXPD data (Supplementary Fig. 14 and Supplementary Notes (Interaction between GVL and Nb/Al/H sites)). All datasets enabled the direct observation of two independent binding sites for GVL (I and II) within the pores (weighted profile factor of 4–6%; Fig. 4, Supplementary Fig. 15 and Supplementary Tables 7–12) without a notable structural phase change of the framework (Supplementary Fig. 14). GVL^{I} and GVL^{II} are located near the intersection of straight and sinusoidal channels, respectively (Fig. 4a–c). Importantly, the adsorbed GVL molecules showed three distinct spatial orientations within the framework of HZSM-5, NbS-1 and NbAlS-1, which indicates the presence of varying host–guest interactions. In the straight channel of HZSM-5, GVL^{I} interacts with a bridging O(H) centre through its C=O group (C=O•••O = 3.812(54) Å) via a weak hydrogen bond (Fig. 4d). In NbS-1, GVL^{I} directly binds to framework T sites (NbO_4 moieties) via its intra-ring O centre (T•••OC_4 = 4.005(39) Å) (Fig. 4e). Interestingly, the adsorbed GVL^{I} in NbAlS-1 forms host–guest interactions with both bridging O(H) centres and T sites (C=O•••O = 3.574(141) Å and Nb•••OC_4 = 3.789(75) Å) (Fig. 4f). Similar, but more notable, observations were observed for GVL^{II} (Fig. 4g–i). For example, GVL^{II} forms a weak hydrogen-bond interaction to a bridging O(H) centre (C=O•••O = 3.210(38) Å) in HZSM-5 and a dipole interaction to the framework T site (Nb•••OC_4 = 3.560(40) Å) in NbS-1, whereas in NbAlS-1, it displays a combination of these two types of interactions (C=O•••O = 3.055(57) Å and Nb•••OC_4 = 3.490(75) Å]. These results strongly indicate that Brønsted or Lewis acid sites alone in HZSM-5 or NbS-1 can only serve as 'monodentate' binding sites for GVL molecules, whereas the cooperativity between these two types of acid sites results in the optimal adsorption of GVL via a 'chelating' mechanism in NbAlS-1. Recently, the distribution of SiO(H)Al sites in LTA zeolite was studied using periodic DFT calculations and INS[40,41]. Here, ^{29}Si NMR, INS and DFT calculations demonstrate the presence of $NbO(SiO)_nAl$ (n = 1 or 2) species in NbAlS-1, which promotes the preferred adsorption of GVL in NbAlS-1 (Supplementary Figs. 16–18, Supplementary Tables 13–15 and Supplementary Notes (Distribution of Nb/Al/H sites)). Thus, the excellent catalytic activity of NbAlS-1 for butene production originates from (1) the highly confined adsorption of GVL in the framework pores and (2) the greatly reduced Brønsted acidity of the resultant framework (~70% compared to HZSM-5), which lead to the rapid desorption of butene products from the catalyst surface, and thus prevent their further reaction to form various cyclic by-products and cokes.

Studies of reaction mechanism

Combined INS and DFT calculations were applied to investigate the vibrational dynamics of GVL@NbAlS-1(0.027/0.04/1) in operando. Recently, this technique was employed to investigate the vibrational dynamics of 1-octene@ZSM-5 (ref. [42]). The INS spectra of solid and adsorbed GVL were recorded and modelled via DFT calculations (Fig. 5a,b, Supplementary Figs. 19–23, Supplementary Table 16 and Supplementary Notes (Inelastic neutron scattering)), which allowed a full assignment of the spectral features for GVL. Comparison of the INS spectra of adsorbed GVL (spectrum of empty cell has been subtracted) and solid GVL shows a number of observations (Fig. 5a). There is little change in the low-energy modes (<100 cm^{-1}) of GVL on adsorption, which indicates the adsorbed GVL molecules are highly ordered and confined within the framework. The peaks at 1,060 cm^{-1} (assigned to C4–O1 stretching) and at 1,127 cm^{-1} (assigned to C1–O1–C4 asymmetric stretching) decrease significantly in intensity and shift to 1,046 cm^{-1} and 1,121 cm^{-1}, respectively, which indicates that the

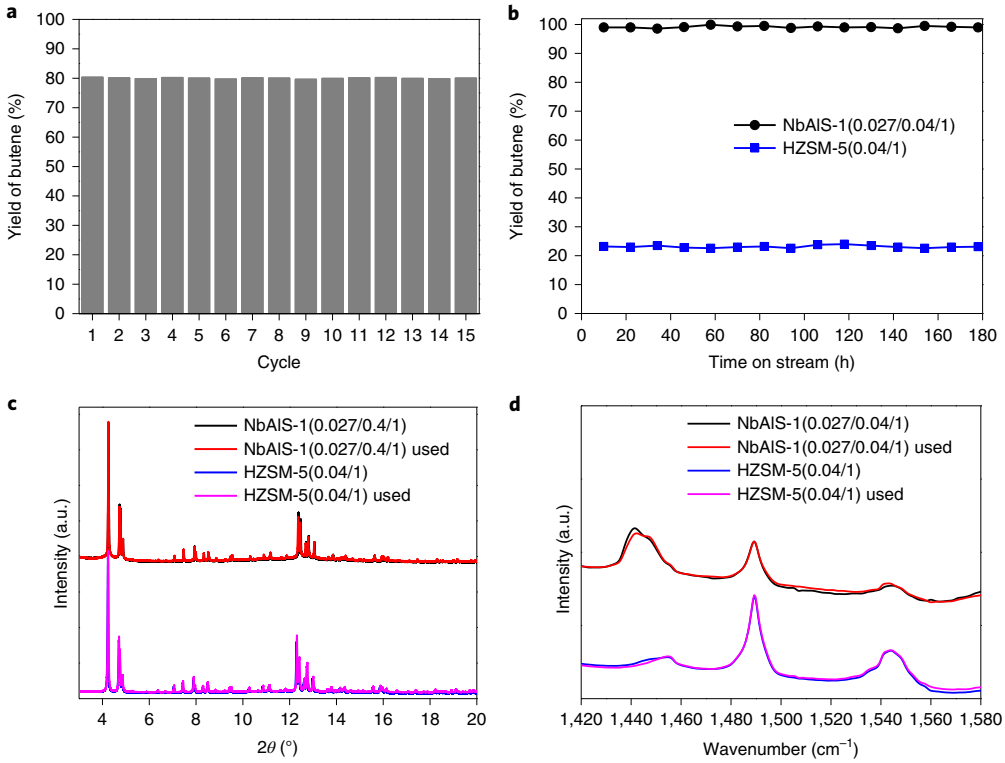

Fig. 2 | Catalyst stability. a, Comparison of butene yield over 15 cycles of reactions over NbAlS-1(0.027/0.04/1) at 320 °C using bulk GVL (99%) as the feed. After each cycle, the catalyst is calcined at 550 °C under an air flow. **b**, Lifetime study of NbAlS-1(0.027/0.04/1) and HZSM-5(0.04/1) at 320 °C using 30 wt% GVL in aqueous solution as the feed. The yield of butene remained at >99% after 180 h of continuous reaction. **c**,**d**, Comparison of SXPD patterns ($\lambda = 0.82487(1)$ Å) (**c**) and acidities determined by Py-IR spectroscopy (**d**) of HZSM-5(0.04/1) and NbAlS-1(0.027/0.04/1) before and after the conversion of 30 wt% GVL at 320 °C for 180 h.

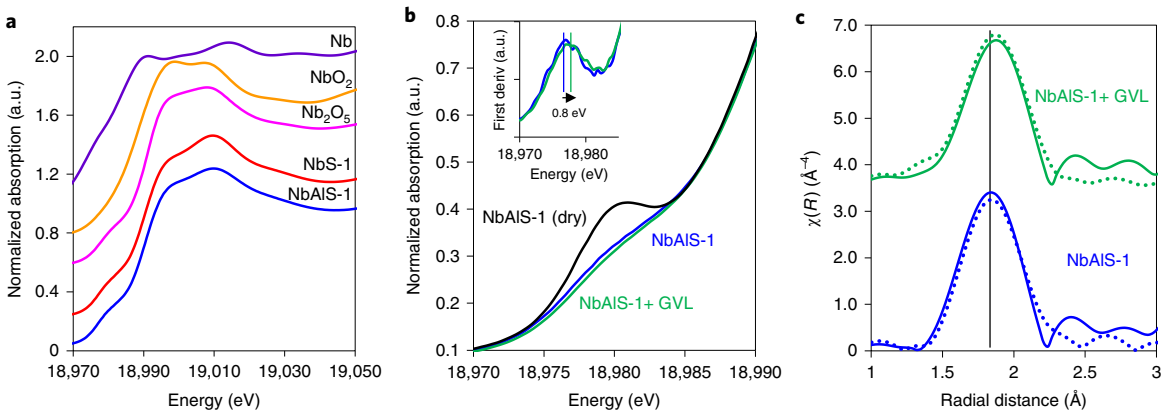

Fig. 3 | Nb K-edge XAS for Nb-containing zeolites. a), X-ray absorption near-edge spectra highlighting both the edge position and pre-edge feature of the Nb-containing samples. **b**, Shifts of pre-edge feature in NbAlS-1, with inset showing the first derivate in the presence of water and GVL substrates. **c**, Phase-corrected, k^3-weighted Fourier transform of the extended X-ray absorption fine structure spectra and fitting curves (dotted lines) for bare and GVL-saturated NbAlS-1. deriv, derivative.

C4–O1 and C1–O1 bonds are activated on adsorption via O1 to the Nb(v) site. Meanwhile, the peaks at 151 cm^{-1} (assigned to C4 out-of-plane wagging) and at 827 cm^{-1} (assigned to ring distortion) also decrease in intensity owing to the hindered motion of O1 on adsorption. The modes of the C4–C5 torsion (273 cm^{-1}) and rocking (317 cm^{-1}) are also affected by adsorption via the O1 centre, and shift to lower energies at 234 and 308 cm^{-1}, respectively. The marked redshift of $\Delta = 39$ cm^{-1} for the torsion mode confirms the restricted motion of the methyl group on adsorption ($-CH_3 \bullet\bullet\bullet O_{zeolite} = 2.032(65)$ Å). The rocking mode of C1=O2 (512 cm^{-1}) disappears completely, consistent with the formation of hydrogen bonds to the Brønsted acid site. The peak at 181 cm^{-1} (assigned to the twisting mode of O2=C1–C2) shifts to 173 cm^{-1}, which further confirms the adsorption of GVL via the O2 centre on the Brønsted acid sites. These findings are highly consistent with the X-ray crystal structures.

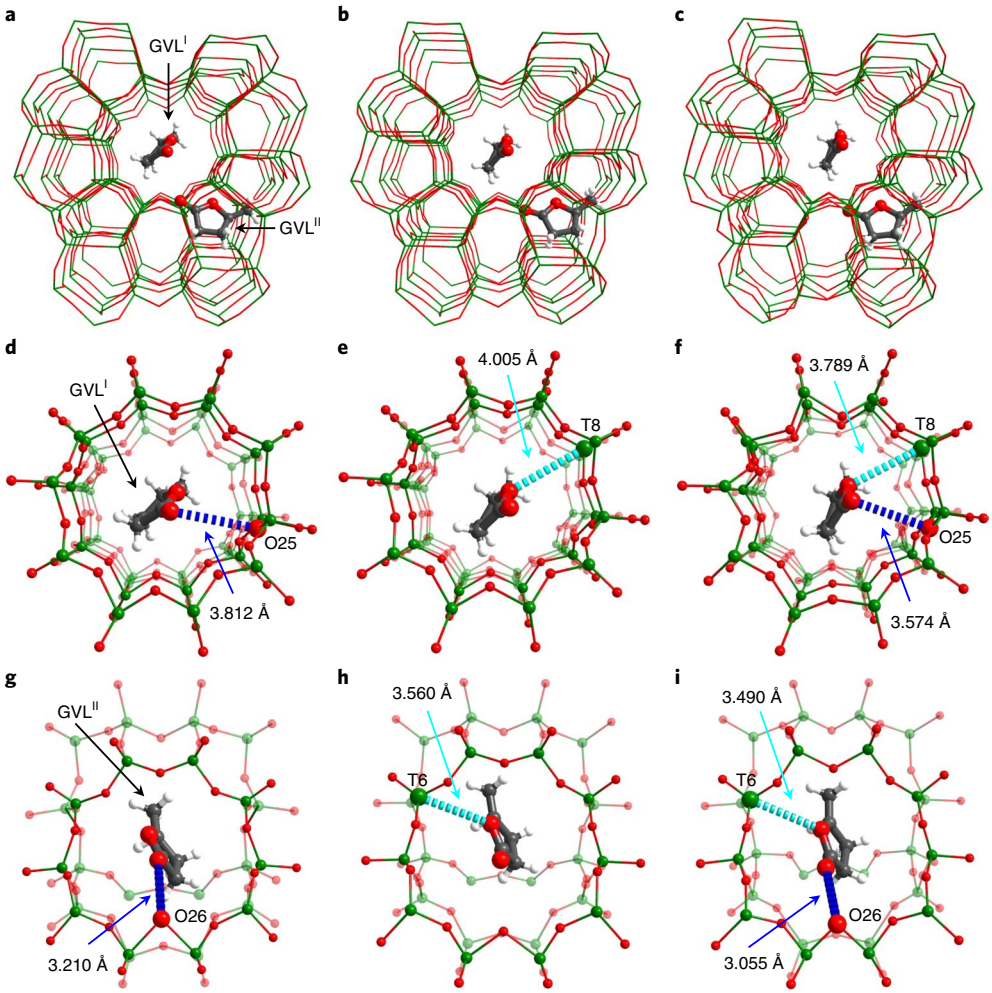

Fig. 4 | Views of crystal structures of GVL-loaded HZSM-5(0.04/1), NbS-1(0.027/1) and NbAlS-1(0.027/0.04/1). All the models were obtained from Rietveld refinements based on in situ SXPD data. Two distinct binding sites for GVL were observed in the straight channel (I) and the sinusoidal channel (II). **a**–**c**, HZSM-5(0.04/1)·8GVL ($Al_{3.692}Si_{92.308}O_{192}$·$8C_5H_8O_2$) (**a**), NbS-1(0.027/1)·8GVL ($Nb_{2.524}Si_{93.476}O_{192}$·$8C_5H_8O_2$) (**b**) and NbAlS-1(0.027/0.04/1)·8GVL ($Al_{3.599}Nb_{2.429}Si_{89.972}O_{192}$·$8C_5H_8O_2$) (**c**). **d**–**i**, Detailed views of the host–guest binding of GVL^{I} (**d**–**f**) and GVL^{II} (**g**–**i**) in HZSM-5(0.04/1), NbS-1(0.027/1) and NbAlS-1(0.027/0.04/1), respectively. The GVL molecules and the functional sites involved in the cooperative binding are highlighted by the use of an amplified ball-and-stick model (Nb/Al/Si, green; C, grey; O, red; H, white). The O1···Nb interactions, O2···O(H) interactions are highlighted in cyan and blue, respectively. Owing to the uncertainty on locations of protons, all hydrogen bonds in this report are described as the distance between the O_{GVL} and the $O_{zeolite}$ centres.

Adsorbed GVL molecules on NbAlS-1(0.027/0.04/1) underwent a first catalytic conversion at 280 °C for three minutes (Fig. 5a). The peaks at 1,046, 1,121 and 827 cm^{-1} (all involve C4–O1 vibrational modes) further reduce in intensity, which indicates that the C4–O1 bond is selectively activated. To promote further conversion, a second reaction was carried out at 300 °C for three minutes (Fig. 5a). All the INS features related to C4–O1 modes (1,046 and 1,121 cm^{-1}) and ring deformation (609, 655, 802, 827 and 899 cm^{-1}) disappeared, which suggests that the ring-opening reaction occurs via selective cleavage of the C4–O1 bond in activated GVL. Meanwhile, O2 is protonated, which leads to the decrease of peak intensities at 530 and 173 cm^{-1} (assigned to C1 and C2 out-of-plane wagging modes, respectively). A final reaction was conducted at 320 °C, and these two peaks (530 and 173 cm^{-1}) disappeared, consistent with the decarboxylation reaction via cleavage of the C1–C2 bond (Fig. 5a). Meanwhile, new features appeared at 212, 229, 254, 366, 407 and 437 cm^{-1}, fully consistent with the formation of butenes (Supplementary Fig. 24).

A full catalytic circle was constructed based on the structural, dynamic and modelling results (Fig. 5c). Over NbAlS-1, the adsorption of GVL occurs on Nb(v) and Brønsted acid sites in a 'chelating mode' via O1 and O2 centres, followed by a ring-opening reaction of activated GVL via selective cleavage of the C4–O1 bond at elevated temperatures. Meanwhile, C1=O2 is protonated via proton transfer from the Brønsted acid sites. On the addition of a H shift in the C_5 skeleton, a β-scission occurs and C1–C2 bond is cleaved to yield butenes and an equimolar CO_2. By contrast, on HZSM-5, both the ring-opening and decarboxylation reactions proceed on the Brønsted acid sites (Fig. 5d). The inability for the intermediate carbocation to desorb from the strong acid sites of HZSM-5 results in its transformation into undesirable by-products of 2-cyclopentenone, aromatics and coke via dehydration, aromatization and coking, respectively.

Outlook

Powerful drivers exist for the development of efficient catalysts to enable the sustainable production of light olefins from biomass to remit our reliance on fossil fuels. NbAlS-1, which integrates both Nb(v) and Al(III) sites into the MFI zeolite framework, demonstrates an excellent catalytic performance to transform biomass-derived

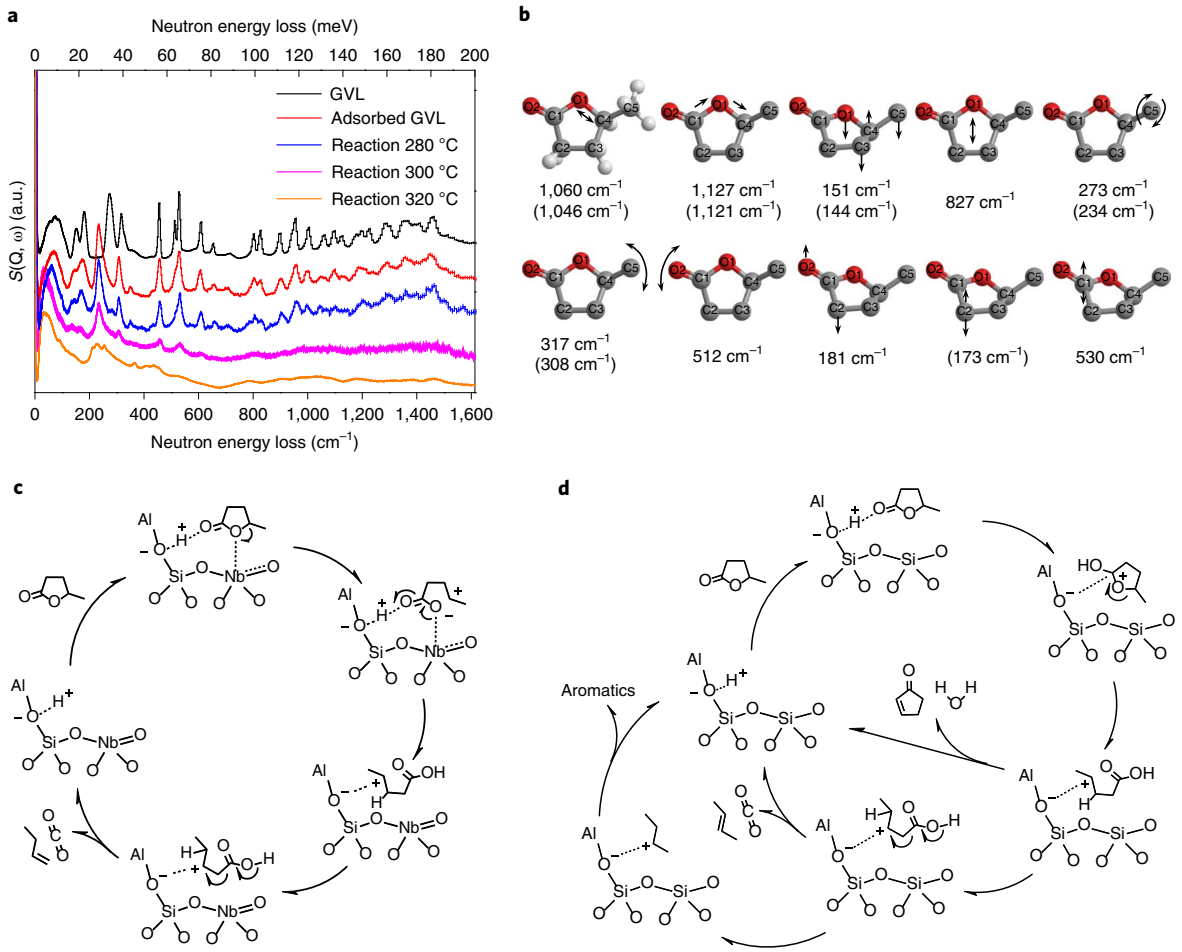

Fig. 5 | INS spectra for NbAlS-1(0.027/0.04/1) on the adsorption and catalytic conversion of GVL and the proposed reaction mechanisms. All the spectra shown here are after the subtraction of the INS spectrum of the empty cell. No abscissa scale factor was used for INS calculations throughout this article. Where no error bars are visible, the error are smaller than the symbols used to represent the data points. **a**, Comparison of INS spectra for condensed solid GVL, adsorbed GVL and reacted GVL on NbAlS-1(0.027/0.04/1). **b**, Selected vibrational modes of GVL. The wavenumbers of adsorbed GVL as observed by experiments are shown in parentheses. For clarification, the hydrogen atoms (white) are only displayed in the first GVL model. **c**,**d**, The proposed reaction mechanisms for the conversion of GVL over NbAlS-1 based on INS/SXPD experiments (**c**) and HZSM-5 based on literature reports (**d**)[13,18,21].

GVL in aqueous solutions into butenes with a quantitative yield. Nb(v) sites in the MFI framework play three vital roles: optimize the acidity of zeolite to hinder the production of by-products, cooperate with Brønsted acid sites for the confined adsorption of GVL and thus activate C–O bonds and resist water poisoning and thus enhance the overall catalytic stability. On reaction completion, the liquid-phase product contains only water and the gas-phase product is an equimolar mixture of butenes and CO_2, which can be facilely separated based on the difference in their boiling points ($\Delta = 72$ °C). While butenes are used as a platform chemical, the recovered CO_2 can be readily sequestrated. The industrial-scale synthesis of NbAlS-1 could be achieved based on the infrastructure widely used for the synthesis of ZSM-5, which, coupled with its high stability, further demonstrates its potential for practical applications.

Online content

Any methods, additional references, Nature Research reporting summaries, source data, extended data, supplementary information, acknowledgements, peer review information; details of author contributions and competing interests; and statements of data and code availability are available at https://doi.org/10.1038/s41563-019-0562-6.

Received: 21 March 2019; Accepted: 11 November 2019;
Published online: 16 December 2019

References

1. Torres Galvis, H. M. & de Jong, K. P. Catalysts for production of lower olefins from synthesis gas: a review. *ACS Catal.* **3**, 2130–2149 (2013).
2. Bender, M. An overview of industrial processes for the production of olefins—C_4 hydrocarbons. *ChemBioEng Rev.* **1**, 136–147 (2014).
3. Galvis, H. M. T. et al. Supported iron nanoparticles as catalysts for sustainable production of lower olefins. *Science* **335**, 835–838 (2012).
4. Amghizar, I., Vandewalle, L. A., Van Geem, K. M. & Marin, G. B. New trends in olefin production. *Engineering* **3**, 171–178 (2017).
5. Jiao, F. et al. Selective conversion of syngas to light olefins. *Science* **351**, 1065–1068 (2016).
6. Zacharopoulou, V. & Lemonidou, A. A. Olefins from biomass intermediates: a review. *Catalysts* **8**, 2 (2018).
7. Tuck, C. O., Pérez, E., Horváth, I. T., Sheldon, R. A. & Poliakoff, M. Valorization of biomass: deriving more value from waste. *Science* **337**, 695–699 (2012).
8. Bozell, J. J. Connecting biomass and petroleum processing with a chemical bridge. *Science* **329**, 522–523 (2010).
9. Bond, J. Q., Alonso, D. M., Wang, D., West, R. M. & Dumesic, J. A. Integrated catalytic conversion of γ-valerolactone to liquid alkenes for transportation fuels. *Science* **327**, 1110–1114 (2010).
10. Jing, Y., Guo, Y., Xia, Q., Liu, X. & Wang, Y. Catalytic production of value-added chemicals and liquid fuels from lignocellulosic biomass. *Chem* **5**, 2520–2546 (2019).

11. Corma, A., Iborra, S. & Velty, A. Chemical routes for the transformation of biomass into chemicals. *Chem. Rev.* **107**, 2411–2502 (2007).
12. Yan, K., Yang, Y., Chai, J. & Lu, Y. Catalytic reactions of *gamma*-valerolactone: a platform to fuels and value-added chemicals. *Appl. Catal. B* **179**, 292–304 (2015).
13. Lin, L. et al. Acid strength controlled reaction pathways for the catalytic cracking of 1-butene to propene over ZSM-5. *J. Catal.* **309**, 136–145 (2014).
14. Hong, E., Park, J.-H. & Shin, C.-H. Oxidative dehydrogenation of *n*-butenes to 1,3-butadiene over bismuth molybdate and ferrite catalysts: a review. *Catal. Surv. Asia* **20**, 23–33 (2016).
15. Ye, L. et al. Decarboxylation of lactones over Zn/ZSM-5: elucidation of the structure of the active site and molecular interactions. *Angew. Chem. Int. Ed.* **56**, 10711–10716 (2017).
16. Shao, H., Lv, Z., Sun, Z., Liu, C. & He, A. Synthesis of spherical polyethylene/poly(1-butene) reactor blends with two-stage sequence polymerization technology. *Polymer* **144**, 72–79 (2018).
17. Kim, M. S., Park, M. S., Seo, H. J. & Lee, S. H. Method for preparing polybutene. US Patent 9683060B2 (2017).
18. Kellicutt, A. B., Salary, R., Abdelrahman, O. A. & Bond, J. Q. An examination of the intrinsic activity and stability of various solid acids during the catalytic decarboxylation of γ-valerolactone. *Catal. Sci. Technol.* **4**, 2267–2279 (2014).
19. Bond, J. Q., Wang, D., Alonso, D. M. & Dumesic, J. A. Interconversion between γ-valerolactone and pentenoic acid combined with decarboxylation to form butene over silica/alumina. *J. Catal.* **281**, 290–299 (2011).
20. Bond, J. Q., Martin Alonso, D., West, R. M. & Dumesic, J. A. γ-Valerolactone ring-opening and decarboxylation over SiO_2/Al_2O_3 in the presence of water. *Langmuir* **26**, 16291–16298 (2010).
21. Bond, J. Q., Jungong, C. S. & Chatzidimitriou, A. Microkinetic analysis of ring opening and decarboxylation of γ-valerolactone over silica alumina. *J. Catal.* **344**, 640–656 (2016).
22. Yun, G.-N., Ahn, S.-J., Takagaki, A., Kikuchi, R. & Oyama, S. T. Hydrodeoxygenation of γ-valerolactone on bimetallic NiMo phosphide catalysts. *J. Catal.* **353**, 141–151 (2017).
23. Lin, W.-C. et al. Zinc-incorporated microporous molecular sieve for mild catalytic hydrolysis of γ-valerolactone: a new selective route for biomass conversion. *ChemSusChem* **11**, 4214–4218 (2018).
24. Serrano-Ruiz, J. C., Braden, D. J., West, R. M. & Dumesic, J. A. Conversion of cellulose to hydrocarbon fuels by progressive removal of oxygen. *Appl. Catal. B* **100**, 184–189 (2010).
25. Okuhara, T. Water-tolerant solid acid catalysts. *Chem. Rev.* **102**, 3641–3666 (2002).
26. Nakajima, K. et al. $Nb_2O_5{\cdot}nH_2O$ as a heterogeneous catalyst with water-tolerant Lewis acid sites. *J. Am. Chem. Soc.* **133**, 4224–4227 (2011).
27. Zhang, Y. et al. Direct conversion of biomass-derived carbohydrates to 5-hydroxymethylfurfural over water-tolerant niobium-based catalysts. *Fuel* **139**, 301–307 (2015).
28. Zhang, Y. et al. Mesoporous niobium phosphate: an excellent solid acid for the dehydration of fructose to 5-hydroxymethylfurfural in water. *Catal. Sci. Technol.* **2**, 2485–2491 (2012).
29. Takagaki, A., Tagusagawa, C. & Domen, K. Glucose production from saccharides using layered transition metal oxide and exfoliated nanosheets as a water-tolerant solid acid catalyst. *Chem. Commun.* **14**, 5363–5365 (2008).
30. Carniti, P., Gervasini, A., Biella, S. & Auroux, A. Niobic acid and niobium phosphate as highly acidic viable catalysts in aqueous medium: fructose dehydration reaction. *Catal. Today* **118**, 373–378 (2006).
31. Carniti, P., Gervasini, A., Bossola, F. & Dal Santo, V. Cooperative action of Brønsted and Lewis acid sites of niobium phosphate catalysts for cellobiose conversion in water. *Appl. Catal. B* **193**, 93–102 (2016).
32. Nowak, I. & Ziolek, M. Niobium compounds: preparation, characterization, and application in heterogeneous catalysis. *Chem. Rev.* **99**, 3603–3624 (1999).
33. Serrano-Ruiz, J. C., Wang, D. & Dumesic, J. A. Catalytic upgrading of levulinic acid to 5-nonanone. *Green. Chem.* **12**, 574–577 (2010).
34. Xia, Q. et al. Direct hydrodeoxygenation of raw woody biomass into liquid alkanes. *Nat. Commun.* **7**, 11162 (2016).
35. Shao, Y. et al. Selective production of arenes via direct lignin upgrading over a niobium-based catalyst. *Nat. Commun.* **8**, 16104 (2017).
36. Prakash, A. M. & Kevan, L. Synthesis of niobium silicate molecular sieves of the MFI structure: evidence for framework incorporation of the niobium ion. *J. Am. Chem. Soc.* **120**, 13148–13155 (1998).
37. Wichterlová, B., Nováková, J. & Prášil, Z. Structure of defects in γ-irradiated ZSM-5 and Y zeolites: an ESR study. *Zeolites* **8**, 117–121 (1988).
38. Corma, A., Llabrés i Xamena, F. X., Prestipino, C., Renz, M. & Valencia, S. Water resistant, catalytically active Nb and Ta isolated Lewis acid sites, homogeneously distributed by direct synthesis in a beta zeolite. *J. Phys. Chem. C* **113**, 11306–11315 (2009).
39. Duereh, A., Sato, Y., Smith, R. L. & Inomata, H. Analysis of the cybotactic region of two renewable lactone–water mixed-solvent systems that exhibit synergistic Kamlet–Taft basicity. *J. Phys. Chem. B* **120**, 4467–4481 (2016).
40. Lemishko, T., Valencia, S., Rey, F., Jiménez-Ruiz, M. & Sastre, G. Inelastic neutron scattering study on the location of Brønsted acid sites in high silica LTA zeolite. *J. Phys. Chem. C* **120**, 24904–24909 (2016).
41. Lemishko, T. et al. Inelastic neutron scattering study of the aluminum and Brønsted site location in aluminosilicate LTA zeolites. *J. Phys. Chem. C* **122**, 11450–11454 (2018).
42. Hawkins, A. P. et al. Investigation of the dynamics of 1-octene adsorption at 293 K in a ZSM-5 catalyst by inelastic and quasielastic neutron scattering. *J. Phys. Chem. C* **123**, 417–425 (2019).

Methods

Catalyst preparation. HZSM-5 samples were purchased from Alfa Aesar and are denoted as HZSM-5(Al/Si mole ratio). NbAlS-1 and NbS-1 samples were prepared by hydrothermal synthesis, and denoted as NbAlS-1(Nb/Al/Si mole ratio) and NbS-1(Nb/Si mole ratio), respectively. In a typical synthesis, aluminium isopropoxide (99.99+% trace metals basis; Sigma Aldrich) was first dissolved in deionized water, into which tetrapropylammonium hydroxide solution (TPAOH, 1.0 M in H_2O; Sigma Aldrich) as the structure-directing agent was added. The mixture was stirred at room temperature for 2 h, then niobium ethoxide (99.95% trace metals basis; Sigma Aldrich) was added and the mixture stirred for another 2 h. Next, tetraethyl orthosilicate (98%; Sigma Aldrich) was added dropwise and the mixture was stirred for another 2 h, which resulted in a gel with a chemical composition of 1Si:xAl:yNb:0.25TPAOH:15H_2O (x and y were determined by the target Al/Si and Nb/Si mole ratios, respectively). The gel was transferred into a 46 ml Teflon-lined stainless-steel autoclave, which was sealed and heated at 170 °C for 48 h. The solid products were centrifuged, washed with deionized water, dried overnight at 80 °C and finally calcined at 550 °C under air flow for 6 h. NbS-1 samples were synthesized by the same procedure, but without the addition of aluminium isopropoxide. Except for the yield (30%) of NbAlS-1(0.04/0.027/1), typical yields of all the zeolites in this study were 90–95%. $NbOPO_4$ was synthesized by a hydrothermal method at pH = 2 according to the literature[28]. Nb_2O_5 and $Nb_2O_5{\cdot}nH_2O$ samples were purchased from Sigma Aldrich and CBMM, respectively. The methods of zeolite characterization are described in detail in Supplementary Methods (Catalyst characterization).

Catalytic testing. Catalytic reactions were carried out in a stainless-steel continuous-flow reactor (12.7 mm internal diameter). The catalyst (2 g) was pressed, crushed and sorted into grains by 40–60 meshes, and the grains were then activated at 450 °C for 3 h under a nitrogen flow before the reaction. GVL was injected into the nitrogen flow (50 ml min^{-1}) by a syringe pump (Cole-Parmer) and passed through the reactor at the target temperature. The output liquid products were collected and analysed with an Agilent 7890B gas chromatograph equipped with a HP-5 column (30 m × 0.32 mm × 0.25 μm) and an Agilent 6890N–Agilent 5973 N gas chromatograph–mass spectrometer (GC–MS) equipped with a HP-5MS column (30 m × 0.25 mm × 0.25 μm). The output gas products were collected and analysed with an Agilent Micro GC 490 equipped with a PoraPLOT U column (length 10 m) and Agilent 7890A–Agilent 5975 C GC–MS equipped with a HP-PLOT/Q column (30 m × 0.53 mm × 40 μm). GVL conversion was calculated by the equation GVL conversion = $(GVL_{in} - GVL_{out})/GVL_{in} \times 100\%$, where GVL_{in} and GVL_{out} denote the moles of GVL in the feed and exit, respectively. The product selectivity was calculated on a carbon basis, that is, $S_i = (a_i \times n_i)/(\Sigma(a_i \times n_i)) \times 100\%$, where a_i and n_i denote the carbon number and mole of product i, respectively. CO_2 was excluded in the selectivity calculation. The product yield was calculated by the equation yield = conversion × selectivity × 100%. The total carbon balances for the production from GVL typically closed to within 5%.

XAS. Transmission Nb K-edge X-ray absorption spectra were collected on beamline B18 at Diamond Light Source, using a water-cooled Si(311) double crystal monochromator and double toroidal Pt-coated mirror for beam focusing. Data collection spanned 200 eV before the edge to 1,000 eV above it, with a step size of 0.5 eV; for reference, Nb foil spectra were simultaneously collected to enable energy calibrations. GVL-saturated samples were collected as a slurry, contained within a sealed Kapton capillary. Data processing was carried out in the Demeter open source software package, version 0.9.26, with XAS spectra processing (normalization and background subtractions) and extended X-ray absorption fine structure fitting conducted within the Athena and Artemis programs, respectively, within Demeter. Reference niobium oxide standards, NbO_2 and Nb_2O_5, were also collected after dilution in boron nitride.

High-resolution SXPD and Rietveld refinement. SXPD data were collected on Beamline I11, Diamond Light Source (wavelength = 0.824869(10) Å) at room temperature. The zeolite powder was loaded in a 0.7 mm borosilicate glass capillary. High-resolution diffraction data were obtained from the samples using the multi-analyser crystal detectors. The patterns were collected in the 2θ range 0–150° with 0.001° data steps. Using the TOPAS software, the SXPD patterns were refined by the Rietveld methods. The Thompson–Cox–Hastings pseudo-Voigt peak function[43] was applied to describe the diffraction peaks. The scale factor and lattice parameters were allowed to refine for all the diffraction patterns. The refined structural parameters include the fractional coordinates (x, y, z) and isotropic displacement factors for all the atoms, and the site occupancy factors for all the Nb, Al, Si species and GVL molecules. The quality of the Rietveld refinements was assured with low goodness-of-fit factors, low weighted profile factors and well-fitted patterns with reasonable isotropic displacement factors within experimental errors.

INS. INS spectra were recorded on the VISION spectrometer at Spallation Neutron Source, Oak Ridge National Laboratory, as well as on the TOSCA spectrometer at the ISIS Facility at the STFC Rutherford Appleton Laboratory. Both VISION and TOSCA are indirect geometry crystal analyser instruments that provide a wide dynamic range with high resolution. All the INS spectra were collected after the sample was cooled and stabilized at temperatures below 15 K.

The adsorption/reaction experiments were conducted at beamlines TOSCA and VISION and the results obtained from both spectrometers are consistent. In a typical experiment, the catalyst (~11 g) was loaded into a flow-type stainless-steel cell that can also be used as a static cell with all the valves closed. The sample was heated to 450 °C (5 °C min^{-1} ramping) under He for 3 h to remove any remaining trace water before the experiment. Then 20 mmol of GVL was injected into the cell at 135 °C. Before the data collection, the cell was flushed using dry He to remove weakly bound GVL molecules. The samples were cooled to <15 K during the data collection. After each reaction, the cell was flushed with dry He, sealed and cooled for INS collection to detect the presence of possible reaction intermediates. The INS spectra of pure solid compounds for both starting material and reaction products were collected at 5 K. The methods of DFT calculations and modelling of the INS spectra are given in Supplementary Methods (DFT calculations and modelling of the INS spectra).

Data availability

All the relevant data are available from the authors, and/or are included with the manuscript.

References

43. Thompson, S. P. et al. Beamline I11 at Diamond: a new instrument for high resolution powder diffraction. *Rev. Sci. Instrum.* **80**, 075107 (2009).

Acknowledgements

We thank EPSRC (EP/P011632/1), the Royal Society and the University of Manchester for funding. We thank the EPSRC National Service for EPR Spectroscopy at the University of Manchester. A.M.S. thanks the Russian Science Foundation (Grant no. 17–73–10320) and Royal Society of Chemistry for funding. We are grateful to Oak Ridge National Laboratory (ORNL), the ISIS Facility and Diamond Light Source (DLS) for access to the beamlines VISION, TOSCA and I11, respectively. We acknowledge DLS for the provision of beamtime at B18 (UK Catalysis Hub SP15151, SP24726) and G. Cibin and V. Celorrio for help at B18 beamline. We acknowledge the support of The University of Manchester's Dalton Cumbrian Facility (DCF), a partner in the National Nuclear User Facility, the EPSRC UK National Ion Beam Centre and the Henry Royce Institute. We recognize R. Edge and K. Warren for their assistance during the ^{60}Co γ-irradiation processes. We thank A. Jentys from the Technical University of Munich and ISIS Facility for the measurement of the INS spectrum of isobutene as part of RB20053 experimental proposal. We thank C. Webb for help with GC–MS, D. Moulding for help with Raman spectroscopy and M. Kibble for help at the TOSCA beamline. The computing resources were made available through the VirtuES and the ICE-MAN projects, funded by the Laboratory Directed Research and Development programme and by Compute and Data Environment for Science (CADES) at ORNL.

Author contributions

L.L. and M.F carried out the syntheses and characterization of the zeolite samples. L.L. and X.H. carried out the catalytic tests. L.L., A.M.S., F.T. and E.J.L.M. collected and analysed the EPR data. L.L. and C.M.A.P. collected and analysed the XAS data. L.L., J.H.C., I.D.S. and C.C.T. collected and analysed the synchrotron X-ray diffraction data. Z.T. and Y.L. collected and analysed the Py-IR data. L.L., Y.C., L.L.D., S.R. and A.J.R.-C. collected and analysed the neutron scattering data and carried out the DFT modelling. S.Y. was responsible for the overall direction of the project and preparation of the manuscript, with contributions from all authors.

Competing interests

S.Y. and L.L. are inventors of a patent based on this work.

Additional information

Supplementary information is available for this paper at https://doi.org/10.1038/s41563-019-0562-6.

Correspondence and requests for materials should be addressed to S.Y.